Supplemental Material

Quantum Spin-Valley Hall Kink States: From Concept to Material Design

Tong Zhou[1], Shuguang Cheng[2], Michael Schleenvoigt[3], Peter Schüelgen[3],
Hua Jiang[4], Zhongqin Yang[5], and Igor Žutić [1]

[1]Department of Physics, University at Buffalo, SUNY, Buffalo, NY 14260, USA
[2]Department of Physics, Northwest University, Xi'an 710069, China
[3]Peter Grünberg Institute 9, Forschungszentrum Jülich & JARA Jülich-Aachen Research Alliance, 52425 Jülich, Germany
[4]School of Physical Science and Technology, Soochow University, Suzhou 215006, China
[5]State Key Laboratory of Surface Physics and Key Laboratory of Computational Physical Sciences (MOE) and Department of Physics and Collaborative Innovation Center of Advanced Microstructures, Fudan University, Shanghai 200433, China

I. First-Principles Calculation Methods and Orbital-Resolved Bands

The geometry optimization and electronic structure calculations were performed by using the first-principles method based on density-functional theory (DFT) with the projector-augmented-wave (PAW) formalism, as implemented in the Vienna ab-initio simulation package (VASP) [1]. All calculations were carried out with a plane-wave cutoff energy of 550 eV and 12 × 12 × 1 Monkhorst-Pack grids were adopted for the first Brillouin zone integral. The Perdew-Burke-Ernzerhof generalized-gradient approximation (GGA) was used to describe the exchange and correlation functional [2]. A vacuum space of larger than 15 Å was used to avoid the interaction between two adjacent slabs. The convergence criterion for the total energy is 10^{-6} eV. The conjugated gradient algorithm is employed to perform the structural optimization. All the atoms in the unit cell are allowed to move until the Hellmann−Feynman force on each atom is smaller than 0.01 eV/Å. The lattice constants of Bi/SiC, BiAs/SiC and BiSb/SiC are 5.35 Å, taken from the experiments [3]. The optimized lattice constants of $BiAsH_2$ and $BiAsI_2$ are 5.07 Å and 5.08 Å, respectively. The Berry curvature, $\Omega(\mathbf{k})$ for the whole valence bands are calculated by [4]

$$\Omega(\mathbf{k}) = \sum_n f_n \Omega_n(\mathbf{k}),$$

$$\Omega_n(\mathbf{k}) = -2\,\mathrm{Im}\sum_{m\neq n} \frac{<\psi_{n\mathbf{k}}|\upsilon_x|\psi_{m\mathbf{k}}><\psi_{m\mathbf{k}}|\upsilon_y|\psi_{n\mathbf{k}}>\hbar^2}{(E_m - E_n)^2},$$

where E_n is the eigenvalue of the Bloch functions $|\psi_{n\mathbf{k}}>$, f_n is the Fermi-Dirac distribution function at zero temperature, υ_x and υ_y are the velocity operators. The Z_2 invariant was computed by tracing the Wannier charge centers using the non-Abelian Berry connection as implemented in the WannierTools software [5].

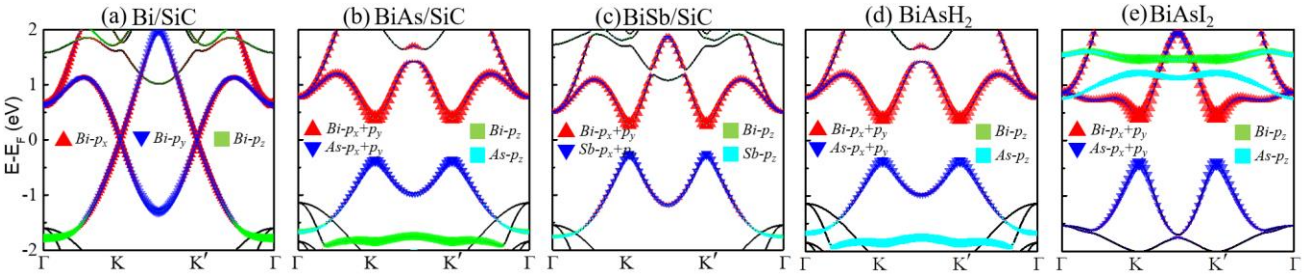

Fig. S1 (a)-(e) Orbital-resolved bands without SOC for Bi/SiC, BiSb/SiC, BiAs/SiC, $BiAsH_2$ and $BiAsI_2$ monolayers, respectively.

The orbital-resolved bands without spin-orbit coupling (SOC) of Bi/SiC, BiAs/SiC, BiSb/SiC, $BiAsH_2$, and $BiAsI_2$ are shown in Fig. S1, where we can clearly see all their bands near the Fermi level are dominated by the p_x and p_y orbitals of Bi, Sb, or As atoms, indicating their low energy electronic structures and topological properties can be well described by our tight-binding (TB) model based on p_x and p_y basis. By fitting the TB model with DFT calculated bands, the intrinsic SOC and staggered potential (λ_{SO}, U) for Bi/SiC, BiAs/SiC, BiSb/SiC, $BiAsH_2$, and $BiAsI_2$ are obtained as (0.44 eV, 0 eV), (0.24 eV, 0.38 eV), (0.30 eV, 0.26 eV), (0.35 eV, 0.37 eV), and (0.44 eV, 0.41 eV), respectively.

II. Conductance Calculations

The conductance of the quantum spin Hall (QSH), quantum-valley Hall kink (QVHK), and quantum-spin-valley Hall kink (QSVHK) states are calculated by employing a two-terminal Landauer-Büttiker formalism based on the Green function technique [6]

$$G_{LR} = \frac{e^2}{h}\mathrm{Tr}[\Gamma_L G^r \Gamma_R G^a],$$

where $G^{r(a)}$ is the retarded (advanced) Green function of the central scattering region, as shown in Fig. S2(a). The terminals are assumed the same as the central region in the absence of disorder. The quantities $\Gamma_{L(R)} = i[\sum^r_{L(R)} - \sum^a_{L(R)}]$ are the linewidth functions describing the coupling between the left (right) terminal and the central scattering region, where $\Sigma^{r(a)}$ is the retarded (advanced) self-energy due to the L(R) semi-infinite lead, and can be numerically obtained via a transfer matrix method [7].

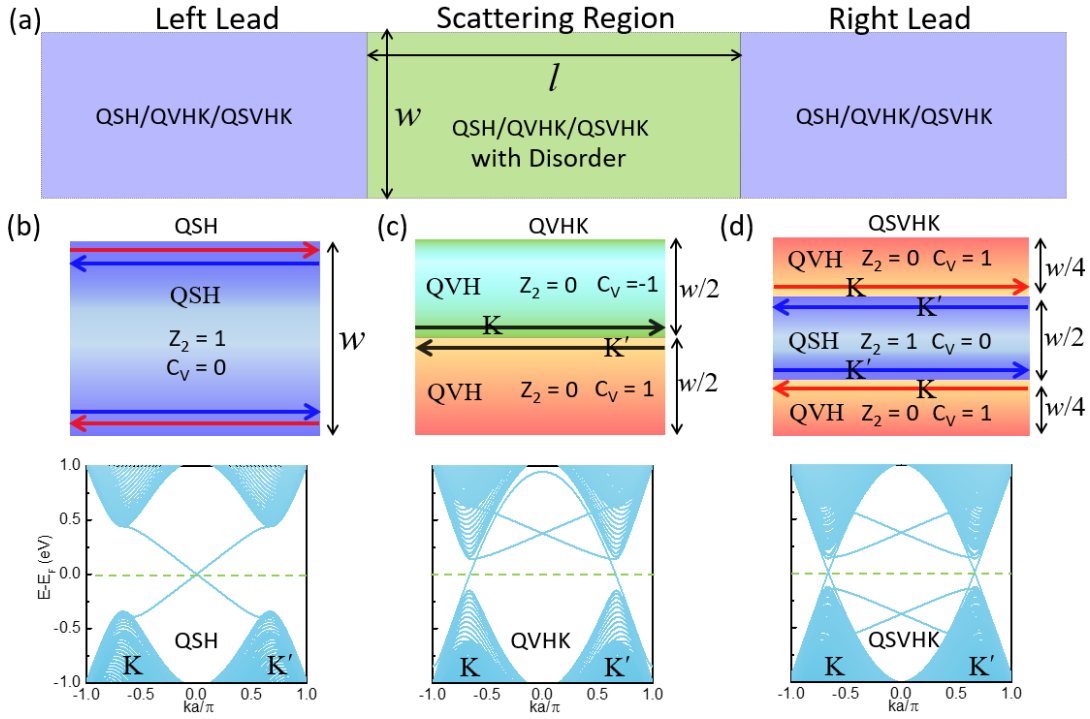

Fig. S2 (a) Two-terminal model for conductance calculations. (b)-(c) The schematic (top) and calculated bands (bottom) for QSH, QVHK and QSVHK states, respectively. The parameters (λ_{SO}, U) of (0.44 eV, 0 eV), (0.24 eV, 0.38 eV) and (0.24 eV, -0.38 eV) obtained from Bi/SiC, BiAs/SiC, and AsBi/SiC, are used for QSH, QVH (C_V=1), and QVH (C_V=-1) regions, respectively. The length (l) and width (w) of the scattering region are 100 and 200 unit cells, corresponding to 46 nm and 92 nm, respectively. The hopping parameter $t_{1,2}$ is set to be 1eV.

For the QSH states, the conductance calculations are based on the bands of Bi/SiC in Fig. S2(b). For QVHK states, we construct a BiAs-AsBi/SiC junction with Cv = 1 (-1) in the BiAs/SiC (AsBi/SiC) region, where the spin-degenerate kink states appear along the interface as shown in Fig. S2(c). The conductance of the QSVHK states is calculated based on the BiAs-Bi-BiAs/SiC junction as shown in Fig. S2(d). The Fermi level, E_F is 0 in all conductance calculations. The disorder is added in the scattering region (See details in Sec. IV). For each value of the disorder strength, 200 disorder configurations are averaged.

III. Rashba Spin-Orbit Coupling

Considering Rashba SOC can be induced into bismuthene by the SiC substrate [3], here we explore its influence on QSVHK states. The Rashba SOC in Bi/SiC is described by H_R based on a TB model in the basis of p_x and p_y orbitals with [3, 8, 9]

$$H_{\mathrm{R}} = \sum_{i} \sum_{j=1,2,3} c_i^{+} T_{R\delta_j} c_{i+\delta_j} + H.C.$$

Here, c_i represents the annihilation operator on site $\boldsymbol{i}$. $T_{R\delta}$ describes the nearest hopping from site $\boldsymbol{i}$ to $\boldsymbol{i} + \boldsymbol{\delta_j}$, which is induced by the extrinsic Rashba SOC from the SiC substrate with

$$T_{R\delta_j} = (-1)^{j+1} i \begin{bmatrix} \lambda_R & z^{(3-j)}\lambda_R^{'} \\ z^{j}\lambda_R^{'} & \lambda_R \end{bmatrix} \otimes [s_x \sin(\frac{3-j}{3})\pi - s_y \cos(\frac{3-j}{3})\pi],$$

where $z = \exp(2i\pi/3)$, λ_R and λ'_R reflect the Rashba SOC strength with $\lambda'_R = \lambda_R t_2/t_1$, and s indicates the Pauli matrices acting on the spin space. By fitting the TB bands including Rashba SOC with DFT calculated bands [Fig. 3], we obtain λ_R of 30 meV for Bi/SiC, which is consistent with the previous work [3]. Similarly, λ_R of 28 meV is obtained for BiAs/SiC system.

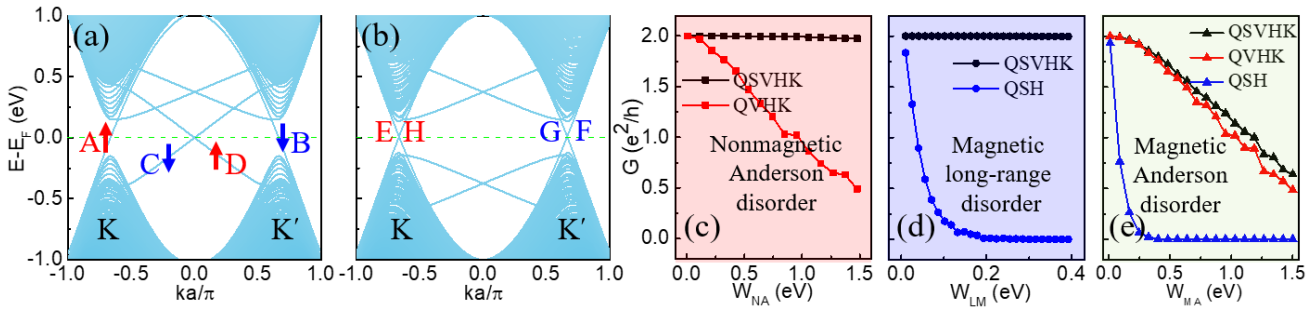

Fig. S3 (a) - (e) same as Figs. 2 (a) - (e), but with Rashba SOC of λ_R = 30 meV, respectively.

Since Rashba SOC does not change the valley-inversion symmetry (VIS) and time-reversal symmetry (TRS), and its strength λ_R is much smaller compared to U and λ_{SO} in the BiAs-Bi/SiC system, it is expected the Rashba SOC does not affect much the results. Indeed, as shown in Figs. S3(a) and (b), the bands with Rashba SOC are nearly the same as the corresponding bands without Rashba SOC [Figs. 2(a) and (b)]. Furthermore, there is no obvious difference between the QSVHK conductance with and without Rashba SOC in the presence of disorder, as shown in Figs. S3(c)-(e) compared to those in Figs. 2(c)-(e). Specifically, the conductance of QSVHK states remain quantized against the nonmagnetic Anderson disorder and magnetic long-range disorder with the consideration of Rashba SOC. Thus, it is reasonable to neglect the influence of Rashba SOC in QSVHK states for BiAs-Bi/SiC system.

IV. Influence and Crossover of the Short-Range and Long-Range Disorder

For valley-related transport, the influence of the short- and long-range disorder is usually significantly different since the former (later) induces (excludes) intervalley scattering, which has been well explored in graphene [10]. The short (long)-range disorder is characterized by the smaller (larger) disorder correlation length, λ, compared to the lattice spacing, a [10, 11]. Their crossover can be well described by a Gaussian correlated disorder potential of $\eta(r) = \omega e^{-r^2/\lambda^2}$, where ω parametrizes the disorder strength [10, 11]. Specifically, for a short-range disorder, usually induced by the point defects [10], its disorder potential localizes in the atomic range ($\lambda < a$) and the induced intervalley scattering enables strong backscattering, eventually turning the conducting system into an Anderson insulator. Such a short-range disorder is also called Anderson disorder, when $\lambda \to 0$ [10, 11]. In contrast, for a long-range disorder, often arising from the charged impurities or ripples [10], its disorder potential is smooth on the scale of the lattice spacing ($\lambda > a$) and there is very little intervalley scattering. As a result, the back scattering is suppressed and the system remains highly conductive [10, 11].

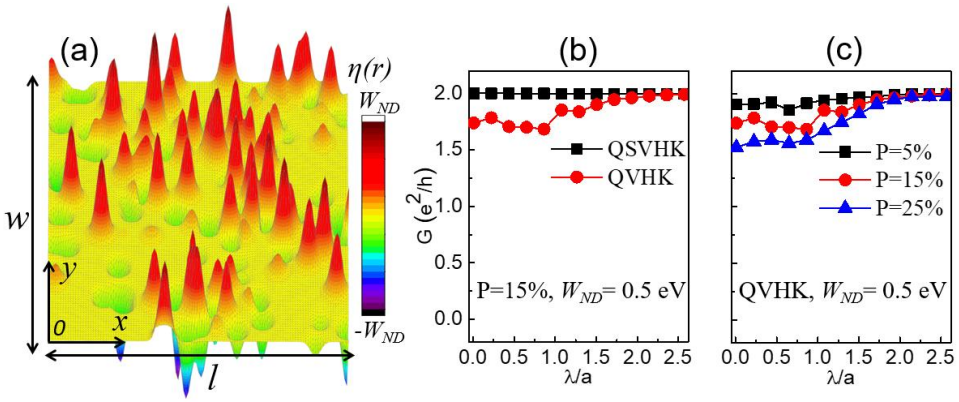

Fig. S4. (a) An example of a realization of the $\eta(r)$ in 2D system. (b) Conductance, G, as a function of the correlation length, λ, for the QVHK and QSVHK states with $\eta(r)$ as in (a), where the disorder probability P = 15% and the disorder strength W_{ND} = 0.5 eV. (c) Same as (b) but for QVHK with various P. In conductance calculations, the width (w) and length (l) of the scattering region are 120 and 2000 unit cells, respectively. Other parameters are taken from Fig. S2.

To explore the influence of the short-range and long-range disorder in our proposed QSVHK states, we add a nonmagnetic disorder term [12] $H_{ND} = \sum_i c_i^+ \eta_i \begin{bmatrix} 1 & 1 \\ 1 & 1 \end{bmatrix} \otimes \sigma_0 c_i$ to Eq. (1). Here, we rewrite $\eta(r)$ in a discrete model as $\eta_i = \sum_{j=1}^{Np} \omega_j e^{-|r_{ij}/\lambda|^2}$, where $|\boldsymbol{r}_{ij}|$ is the distance between site i and j, N_p is the total number of the scattering centers, which, dividing the total number (N) of the lattice sites, gives the disorder probability, P = N_p/N. Figure S4(a) shows the realization of the $\eta(r_i)$. For the short-range disorder, we consider the Anderson disorder (λ = 0) with P = 100%, where ω_j is randomly distributed in [$-W_{NA}$, W_{NA}] with W_{NA} the nonmagnetic Anderson disorder strength. By employing Landauer-Büttiker formalism with the Green function technique in a two-terminal model as in Fig. S2, we calculate the QSVHK conductance, G, as a function of W_{NA} shown in Fig. 2(c) in the Main Text. For comparison, we also calculate G(W_{NA}) of QVHK states there. Since QVHK states require the absence of the intervalley scattering, it can only be robust against the long-range disorder. When there exists a short-range disorder, the valley inversion symmetry is broken and the intervalley scattering is easily induced. Thus, its conductance decreases from the quantization as shown in Fig. 2(c). For our proposed QSVHK, because of the additional protection from the QSH, it is not influenced by the intervalley scattering and thus remains robust against nonmagnetic short-range disorder [Fig. 2(c)].

To explore the crossover of the short-range and long-range disorder in the QSVHK, we induce the magnetic short/long-range disorder [13] to break the TRS and thus validating the intervalley scattering in the QSVHK. When the TRS is broken, the QSVHK degrades into the QVHK, and then it is expected to be robust against the magnetic long-range disorder, but can be intervalley-scattered by the magnetic short-range disorder. The magnetic disorder is induced by adding an in-plane magnetic exchange filed $H_{MD} = \sum_i c_i^+ \eta_i \begin{bmatrix} 1 & 1 \\ 1 & 1 \end{bmatrix} \otimes \sigma_x c_i$ to Eq. (1). Similar to that in nonmagnetic case, for the short-range disorder, we consider the magnetic Anderson disorder (λ = 0 and P = 100%) with W_{MA} the magnetic Anderson disorder strength. While for the magnetic long-range disorder, we consider λ = 7a and P = 1% with W_{LM} the magnetic long-range disorder strength. Through the conductance calculations, we find the QSVHK conductance remains quantized with W_{LM} [Fig. 2(d)], but decreases with W_{MA} [Fig. 2(e)], consistent with our expectations.

It is generally accepted that the critical disorder correlation length, $\lambda_c \sim a$, separates the short- and long-range disorder [10]. However, for a specific system, λ_c may also be related to the electronic structures of the system and the details of the disorder, including its strength and concentration. To identify the λ_c in our proposed bismuthene system, we calculate the QVHK conductance in the presence of the nonmagnetic disorder $\eta(r_i)$ with various λ as shown in Fig. S4(b), where the η is randomly distributed in [$-W_{NA}$, W_{NA}] with W_{NA} the nonmagnetic disorder strength. We can see that for $\lambda < 2a$, $G < 2e^2/h$, indicating there is a finite intervalley scattering, while for $\lambda > 2a$, the conductance is quantized due to the vanishing intervalley scattering. Thus, λ_c is about 2a in bismuthene system with P = 15% and W_{ND} = 0.5 eV. λ_c is slightly increased when P increases, as shown in Fig. S4(c). This can be readily understood since the larger P enhances the possibility of the intervalley scattering, thus requiring a larger λ_c to compensate it.

V. Influence of the Interface Configuration

Based on the analysis of the topological charge, the QSVHK emerges as long as the topological indexes (Z_2 and C_v) change across the interface. Thus, the QSVHK is expected to be insensitive to the detailed interface configurations, reflecting its topological nature and protection. To clearly show such robustness against the interface configurations, we consider various interface situations discussed as follows, including the gradual interface, curved interface and the interfacial defects.

Influence of the gradual interface. In the Main Text, we assume that the QSH-QVH interface is very sharp, where the parameters (λ_{SO}, U) change as a step function. However, in experiments, because of the atom mixing, the interface may not be as sharp but instead form a domain wall (DW) with a finite width (w_D) as shown in Fig. S5(a). Such a DW can be described by a smooth change of the parameters, taking, for example, cosine change as shown in Figs. S5(b) and (c). Figures S5(d)-(f) show the calculated bands of the QVH-QSH-QVH junctions with various w_D. We can see their bands are quite similar and the QSVHK emerges in all cases, regardless of the DW width. However, the localization length of the QSVHK increases as w_D increases, as shown in the calculated spatial local density of the states (LDOS) of the QSVHK in Fig. S5(g), reflecting the DW character. Since the energy spectra are similar for various w_D, it is expected they also show similar transport properties. To verify this, we calculate their conductances based on a two-terminal model [Fig. S5(a)]. As shown in Fig. S5(h), in the clean limit, the conductance is large outside the bulk gap, while it equals to $2e^2/h$ within the gap. Such quantized conductance originates from the QSVHK. Similar G(E) trends for various w_D indicate the transport properties of the QSVHK do not depend on the DW width.

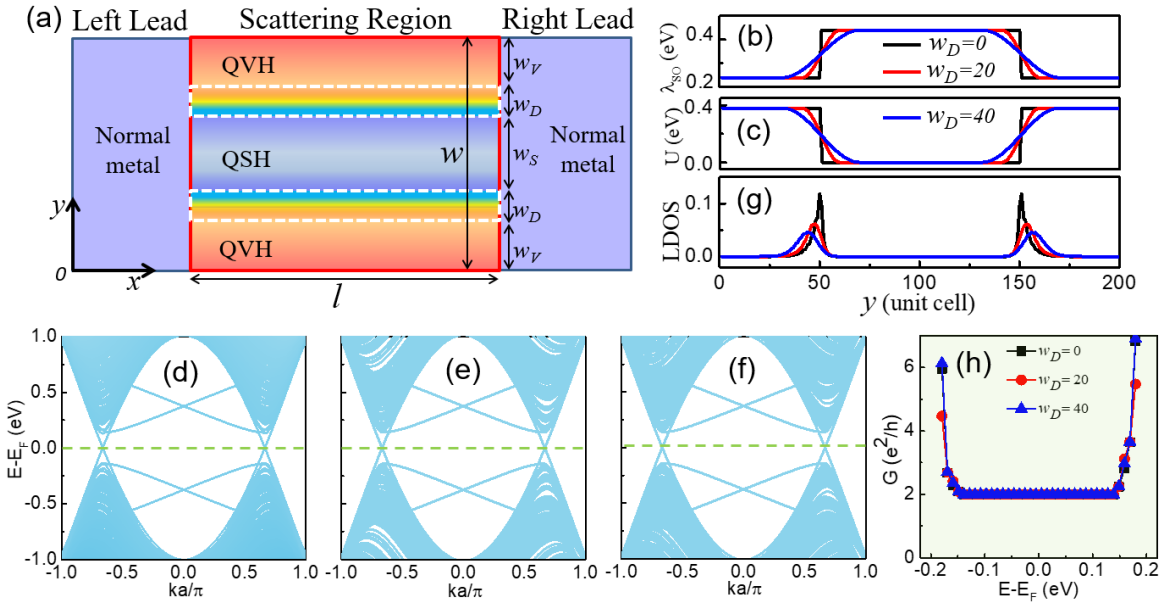

Fig. S5 (a) Two-terminal model for conductance calculations of the QVH-QSH-QVH junctions with domain walls, where w_V, w_S, and w_D indicate the width of the QVH region, QSH region, and domain wall (marked by the white dashed rectangle), respectively. (b) and (c) The parameters of (λ_{SO}, U) change from the QVH region to the QSH region as $\lambda_{SO} = \frac{\lambda_1+\lambda_2}{2} + \frac{\lambda_1-\lambda_2}{2}\cos(\frac{y-y_{L,R}+w_D}{2w_D}\pi)$ and $U = \frac{U_1+U_2}{2} + \frac{U_1-U_2}{2}\cos(\frac{y-y_{L,R}+w_D}{2w_D}\pi)$ with $y_{L,R} - w_D < y < y_{L,R} + w_D$, where y_L=50 (y_R=150) are the center of the left (right) domain walls, $\lambda_{1,2}$ and $U_{1,2}$ are the intrinsic SOC and staggered potential for the QVH and QSH region, taken from the BiAs/SiC and Bi/SiC, respectively. The $w_V = 50 - w_D/2$ and $w_S = 100 - w_D$. (d) - (f) Bands for the scattering region in (a) with w_D = 0, 20, 40 unit cells, respectively. (g) Spatial local density of states (LDOS) for the bands at E_F for (d)-(f). (h) Conductance, G, as a function of the energy E with various w_D for the setup in (a). The l is infinite in band calculations while l =200 unit cells for conductance calculations. Other parameters are taken from Fig. S2 in SM.

Influence of the curved interface. Besides the DW width, the shape of the interface is another important interfacial property. Based on the topological analysis and index theorem, it is expected that the QSVHK states emerge exactly along the interface, regardless of its shape. To illustrate this, we design a curved QSH-QVH interface with sine feature as an example, as shown in Fig. S6(a). The calculated LDOS [Fig. S6(b)] show that the QSVHK exactly flows along the physical interface. Based on similar transport calculations as in Fig. S5, the obtained conductance of the curved interface [Fig. S6(c)] is found to be similar to that of the straight one [Fig. S5(h)]. Especially, the quantized conductance within the gap clearly demonstrates that QSVHK emerges in the curved boundary and its transport properties are insensitive to the shape of the interface.

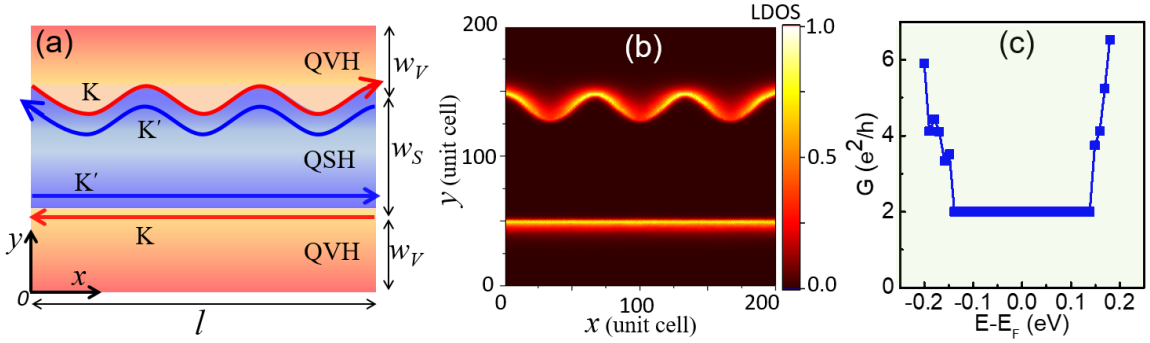

Fig. S6 (a) Schematic of QVH-QSH-QVH junctions with curved interface of 20[1-cos(6$\pi x/l$)]. (b) Spatial LDOS at E_F for the spectrum of (a). (c) Conductance, G, as a function of E for (a) with $l = 2w_S = 4w_V = 200$ unit cells. The parameters are taken from Fig. S5.

Influence of the interfacial defects. Considering the defects can be created around the interface when fabricating the junctions, here we explore the influence of the defects in QSVHK states. As we demonstrated in the Main Text, our proposed QSVHK states are topologically protected by both the valley-inversion and time reversal symmetries. As long as these two symmetries are not simultaneously broken, the QSVHK states can remain robust. As topological states, they are highly robust against the local defects and disorder. Considering the defects in the interface are locally distributed and cannot break the time-reversal symmetry [14, 15], the QSVHK states are expected to be robust against such defects. Encouragingly, a recent study shows even for global defects the quantum spin Hall (QSH) states in bismuthene remain robust when the defect concentration is lower than 17% [15]. Since our proposed QSVHK states are more robust than the QSH states because of the additional protection from the valley-inversion symmetry, the QSVHK states are expected to be robust against the defects.

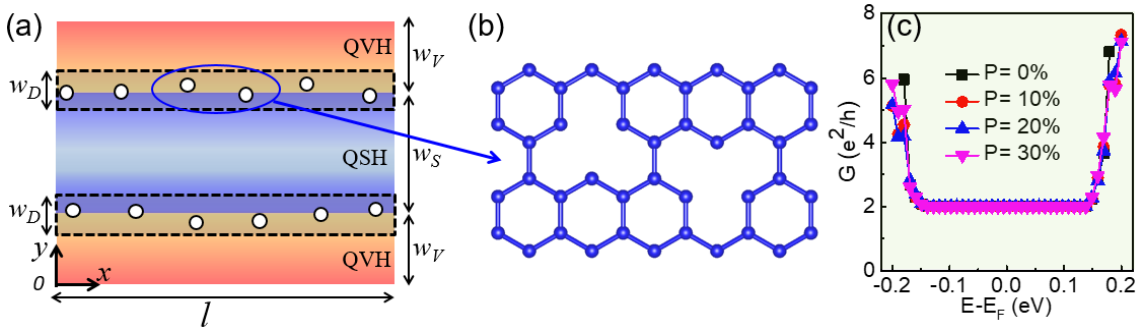

Fig. S7 (a) Schematic of QVH-QSH-QVH junctions with defects marked by the circles around the interface, where the defects are created by randomly removing the atoms in the black dashed rectangle regions with the width w_D = 15 unit cells. The concentration of the defects, P, is defined by the number of the removed atoms over the total number of the atoms in the black dashed rectangle regions. (b) The schematic of the atomic structures with defects for the zoom-in of the area marked by the blue circle in (a). (c) Conductance, G, as a function of E for (a) with various P based on the two-terminal model (Fig. S5), where $l = 2w_S = 4w_V = 200$ unit cells. The other parameters are taken from Fig. S5.

To check our expectations, we create the defects by randomly removing the atoms around the QSH-QVH interface as shown in Figs. S7(a)-(b). Based on similar transport calculations as in Fig. S5, we calculate the conductance, G, as a function of E for (a) with various defect concentrations as shown in Fig. S7(c). We can see the calculated conductance of the junction with finite defect concentrations ($P > 0$) is similar to that with $P = 0$. Specifically, the conductance within the gap remain quantized even when P is up to 30%, clearly demonstrating the QSVHK states are robust against the defects, consistent with our analysis based on the symmetry protections. Such a robustness against the defects additionally facilitates the experimental realization and observation of the QSVHK states.

VI. Influence of the Temperature

For applications of topological states, one key point is that the bulk gap, Δ, remains open, which provides a topological protection for the ballistic transport. However, as commonly expected, the temperature-induced thermal excitation can reduce Δ. A common estimate is that the gap remains open when temperature $T < \Delta/k_B$. For room-temperature applications (300 K), the Δ is required to be larger than 26 meV. Since in our proposed BiAs-Bi/SiC junction Δ ~ 287 meV is 10 times larger than 26 meV, it is reasonable to expect that the QSVHK states in BiAs-Bi/SiC junction can be used at room temperature.

In transport calculations, temperature effects can be simulated by using the Fermi-Dirac distribution function, $f = 1/[1 + \exp\left(\frac{E-E_F}{k_B T}\right)]$, in the conductance calculations, written as [6]

$$G = \frac{2e^2}{h} \int \bar{T}(E)(-\frac{\partial f}{\partial E})dE,$$

where $\bar{T}(E)$ is the transmission coefficient. The calculated temperature-dependent conductance is shown in Fig. S8. We can see the energy range supporting quantized conductance decreases as T increases, reflecting the expected temperature influence. However, when T = 300 K, there is still a visible range of energy supporting ballistic transport, showing a support for the feasibility of the room-temperature applications.

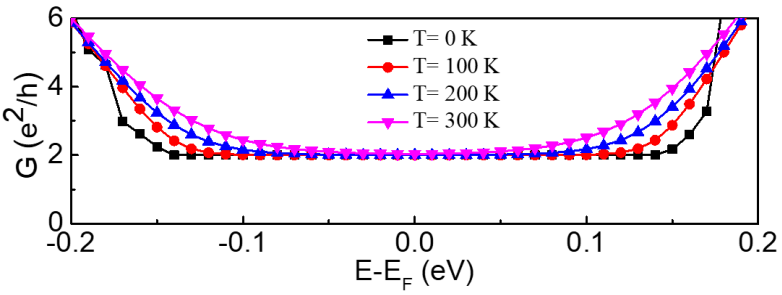

Fig. S8 Temperature-dependent conductance of the QVH-QSH-QVH junction [Fig. S5(a)] as a function of the energy. The parameters are taken from Fig. S5.

The above discussion is based on a single-particle picture, while the electron-electron (e-e) and electron-phonon (e-p) interactions may play important roles at high temperature. Such many-body effects have actually been widely explored in topological states, especially in the QSH system [14]. Since both e-e and e-p interactions induce intervalley scattering [16, 17], the VIS protection for QSVHK states becomes invalid. As a result, the QSVHK degrades into the QSH, which is expected to have a similar behavior as QSH states under electron-electron (e-e) or electron-phonon (e-p) interactions.

For an e-p interaction, since it does not induce spin mixing, the QSH states remain robust when TRS is preserved [17]. For an e-e interaction, it can induce the back scattering in the QSVHK states because both spin and intervalley scattering are allowed even with TRS [14]. However, when the e-e interaction is weak, the QSH states can still remain stable [16, 17]. In typical topological materials (instead of correlated materials), the e-e interactions are usually very weak even at a high temperature [14]. Thus, such many-body interactions have little influence in the QSH states. Besides, the QSH states were detected at 77 K in bismuthene, which is expected to support QSH at room temperature [3]. Since our proposed QSVHK states in BiAs-Bi junction not only share the QSH properties of bismuthene, but also possess an extra protection from the valley-inversion symmetry, it may be reasonable to expect that QSVHK states can survive at room temperature.

VII. Experimental Fabrication

Since the single bismuthene/antimonene/arsenene and their binary films (BiSb and BiAs) have been fabricated [18-19], their planar junctions can be created using our well-established molecular beam epitaxy (MBE) selective area growth and stencil lithography [20]. Specifically, the junction fabrication can be realized in two main steps.

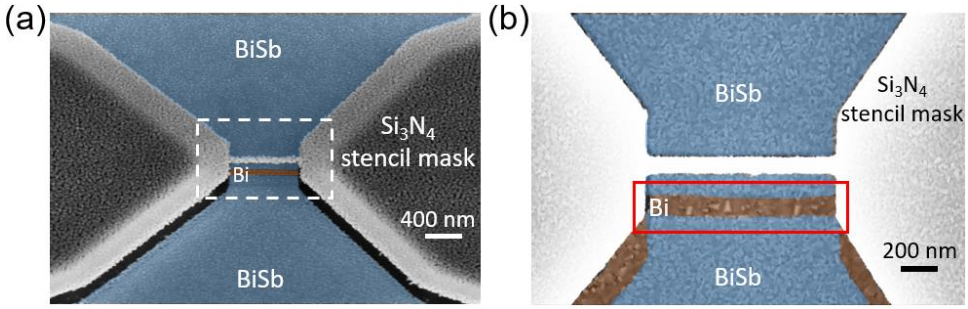

Fig. S9 (a) False color scanning electron micrograph (SEM) image of the planar BiSb-Bi-BiSb junction with a Si_3N_4 stencil mask situated 300 nm above the film for shadowing. (b) The zoom-in of the area marked by the white rectangle in (a), where the BiSb-Bi interfaces are marked by the red rectangle.

I. Fabricating the Si_3N_4 stencil mask for shadowing. Following the process established in our previous work [20], 300 nm of SiO_2 and 100 nm of Si_3N_4 are deposited on a Si (111) substrate via low-pressure chemical vapor deposition (LPCVD). Using electron beam lithography and reactive ion etching, a thin Si_3N_4 stripe as shown in Fig. S9(a) is prepared. Via a following dip into 1% hydrofluoric acid, the SiO_2 under the stripe is etched and the Si_3N_4 bridge is released to create a freestanding bridge. The sample is then transferred into an MBE chamber where it is heated to 700 ℃ to desorb the hydrogen surface passivation. **II.** Spatially-selective growing the BiSb and Bi films. The Bi and Sb are evaporated respectively from standard Knudsen effusion cells at 530 ℃ and 475 ℃ and deposited simultaneously onto the substrate at a growth temperature of 40 ℃, similar to the recipe in [21] but without rotating the substrate. The stoichiometry of Bi and Sb can be flexibly controlled by adjusting the fluxes and growth temperature [21]. Since the Bi and Sb molecular beams have high directionality and reach the substrate from different directions, in the shadow cast by the bridge for each beam respectively only the other element is deposited. With the substrate in a well-defined orientation to the stencil bridge with respect to the Sb source, the BiSb film is grown on the substrate, except for the narrow strip [brown in Fig. S9(a)] shaded by the bridge where only pure Bi film is grown. In this way, a planar BiSb-Bi-BiSb junction is created as shown in Fig. S9(b). The desired BiAs-Bi-BiAs junction can also be fabricated using a similar method.

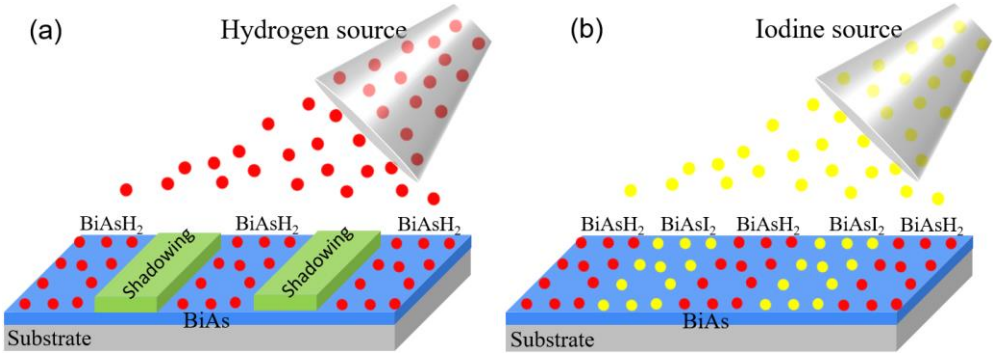

Fig. S10 Schematic of the fabrication of the multiple $BiAsH_2$-$BiAsI_2$ junctions with hydrogen and iodine depositions in (a) and (b).

Relying on the similar techniques, we propose a protocol to fabricate multiple $BiAsH_2$-$BiAsI_2$ junctions based on the fabricated BiAs film as shown in Fig. S10. First, one can attach several shadow masks on the BiAs film and deposit H atoms. Because of the shadow shields, these H atoms are only deposited on the uncovered regions, bonding with the unsaturated p_z orbitals of the Bi/As atoms and forming $BiAsH_2$, as shown in Fig. S10(a). Next, one would remove the shadow masks and deposit the iodine atoms. Since the $BiAsH_2$ regions have been already passivated by the H atoms, the I atoms can only bond with the Bi/As atoms in the non-hydrogentated regions, forming the multiple $BiAsH_2$/$BiAsI_2$ junctions as shown in Fig. S10(b). Such techniques have been widely used in chemistry surface functionalization [18, 19].

VIII. Influence of the Stoichiometry

Since the stoichiometry control is crucial for growing binary-element film using MBE, it is important to explore how the stoichiometry affects the electronic and topological properties of the BiAs films. The two key factors in our proposal are the intrinsic SOC, λ_{SO}, and the staggered potential, U, which are both related to the stoichiometry. Thus, it is expected that the stoichiometry plays a significant role.

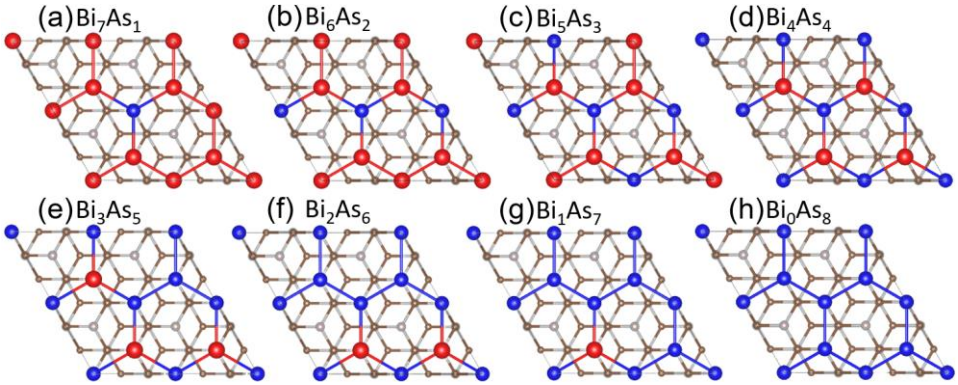

Fig. S11 (a)-(h) Atomic structures of the 2×2 BiAs/SiC supercells with As concentrations from 1/8 to 8/8.

To simulate the influence of the stoichiometry, we created larger 2×2 BiAs/SiC supercells with 1 to 8 As atoms, giving the As-concentration, ρ_{As}, from 1/8 to 8/8, as shown in Fig. S11. The corresponding electronic structures are shown in Figs. S12(b)-(g). By fitting the effective model with such DFT results, the λ_{SO} and U for different ρ_{As} are plotted in Fig. S12(a). We can see the λ_{SO} decreases almost linearly with the ρ_{As}. This is expected since the SOC of As is smaller than that of Bi and the more (less) As (Bi) atoms, the smaller (larger) λ_{SO} is in the BiAs film. For U, Bi_4As_4 gives the maximum U. This can be readily understood since the U indicates the onsite energy difference between the A and B sublattices and the biggest difference emerges when all As (Bi) atoms are at the A (B) sublattice sites, forming the Bi_4As_4 as shown in Fig. S11(d). When some sites of the A (B) sublattice are occupied by the Bi (As) atoms, the U decreases, as in Fig. S12(a). Furthermore, the U vanishes when all sites host the same Bi or As atoms. Such As concentration-dependent competition between U and λ_{SO} determines the gap and topological phase of the BiAs film. Specifically, when $3/8 < \rho_{As} < 6/8$, $U > \lambda_{SO}$, giving the QVH phase. Otherwise, $U < \lambda_{SO}$, giving the QSH phase as shown in Fig. S12(a). Therefore, to get the QSVHK states, the MBE stoichiometry of As:Bi should be controlled in the range from 3:5 to 6:2. Such a large parameter range gives a considerable flexibility for experimental realization of our proposal. In addition to the MBE growth, the BiAs film can also be fabricated from bulk BiAs crystal using exfoliation [18, 19], which may avoid the concern about the stoichiometry control.

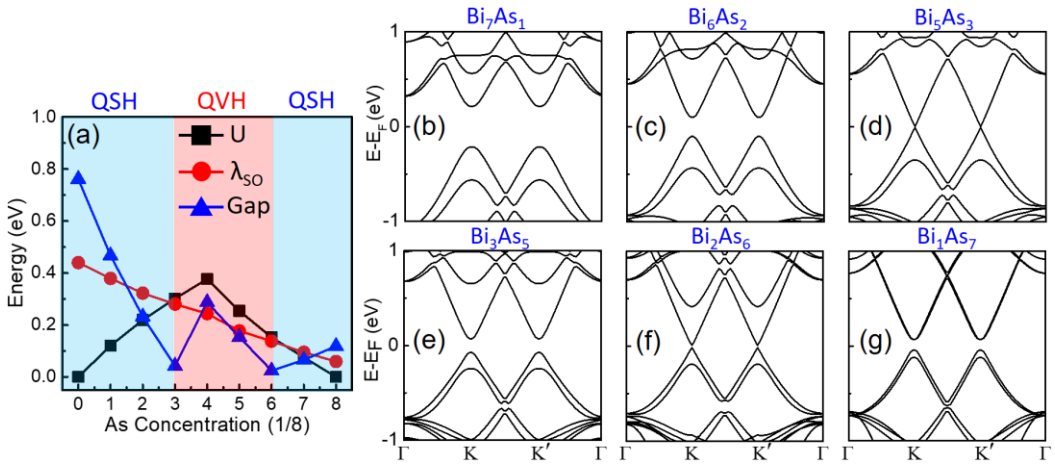

Fig. S12 (a) The As concentration-dependent intrinsic SOC, λ_{SO}, staggered potential, U, and the band gap obtained from the band structures [(b)-(g)] of the corresponding structures in Fig. S11.

The fabricated BiSb-Bi junction and the discussions about the influence of stoichiometry show that our proposed BiAs-Bi junction to realize QSVHK state is promising. The QSVHK states are insensitive to the interface configurations and robust against different nonmagnetic and long-range disorder because of the topological protection. Furthermore, the finite-temperature calculations show the conductance of the QSVHK states remains quantized above room temperature. Taken together, such a strong robustness facilitates the experimental observation of QSVHK states and offers new opportunities in valleytronics and spintronics.

REFERENCES

[1] G. Kresse, and J. Furthmüller, Efficient iterative schemes for ab initio total-energy calculations using a plane-wave basis set, Phys. Rev. B **54**, 11169 (1996).

[2] J. P. Perdew, K. Burke, and M. Ernzerhof, Generalized Gradient Approximation Made Simple, Phys. Rev. Lett. **77**, 3865 (1996).

[3] F. Reis, G. Li, L. Dudy, M. Bauernfeind, S. Glass, W. Hanke,R. Thomale, J. Schafer, and R. Claessen, Bismuthene on a SiC substrate: A candidate for a high-temperature quantum spin Hall material, Science **357**, 287 (2017).

[4] Y. Yao, L. Kleinman, A. H. MacDonald, J. Sinova, T. Jungwirth, D.-S. Wang, E. Wang, and Q. Niu, First Principles Calculation of Anomalous Hall Conductivity in Ferromagnetic bcc Fe, Phys. Rev. Lett. **92**, 037204 (2004).

[5] Q. Wu, S. Zhang, H.-F. Song, M. Troyer, and A. A. Soluyanov, WannierTools: An open-source software package for novel topological materials, Comput. Phys. Commun. **224**, 405 (2018).

[6] S. Datta, Electronic Transport in Mesoscopic Systems (Cambridge University Press, Cambridge, UK, 1997).

[7] M. P. Lopez-Sancho, J. M. Lopez-Sancho, and J. Rubio, Quick iterative scheme for the calculation of transfer matrices: application to Mo (100), J. Phys. F: Met. Phys. **14**, 1205 (1984).

[8] T. Zhou, J. Zhang, Y. Xue, B. Zhao, H. Zhang, H. Jiang, and Z. Yang, Quantum spin-quantum anomalous Hall effect with tunable edge states in Sb monolayer-based heterostructures, Phys. Rev. B **94**, 235449 (2016).

[9] G. Li, W. Hanke, E. M. Hankiewicz, F. Reis, J. Schafer, R. Claessen, C.Wu, and R. Thomale, Theoretical paradigm for the quantum spin Hall effect at high temperatures, Phys. Rev. B **98**, 165146 (2018).

[10] S. Das Sarma, S. Adam, E. Hwang, and E. Rossi, Electronic transport in two-dimensional graphene, Rev. Mod. Phys. **83**, 407 (2011)

[11] A. Rycerz, J. Tworzydło, and C. W. J. Beenakker, Anomalously large conductance fluctuations in weakly disordered graphene, Europhys. Lett. **79**, 57003 (2007).

[12] H. Jiang, L. Wang, Q.-F. Sun, and X. C. Xie, Numerical study of the topological Anderson insulator in HgTe/CdTe quantum wells, Phys. Rev. B **80**, 165316 (2009).

[13] Z. Qiao, Y. Han, L. Zhang, K. Wang, X. Deng, H. Jiang, S. A. Yang, J. Wang, and Q. Niu, Anderson Localization from the Berry-Curvature Interchange in Quantum Anomalous Hall Systems, Phys. Rev. Lett. **117**, 056802 (2016).

[14] X.-L. Qi and S.-C. Zhang, Topological insulators and superconductors, Rev. Mod. Phys. **83**, 1057 (2011).

[15] X. Ni, H. Huang, and F. Liu, Robustness of topological insulating phase against vacancy, vacancy cluster, and grain boundary bulk defects, Phys. Rev. B **101**, 125114 (2020).

[16] C. Xu and J. E. Moore, Stability of the quantum spin Hall effect: Effects of interactions, disorder, and Z_2 topology Phys. Rev. B **73**, 045322 (2006).

[17] J. C. Budich, F. Dolcini, P. Recher, and B. Trauzettel, Phonon-induced backscattering in helical edge states, Phys. Rev. Lett. **108**, 086602 (2012).

[18] S. Zhang, S. Guo, Z. Chen, Y. Wang, H. Gao, J. Gómez- Herrero, P. Ares, F. Zamora, Z. Zhu, and H. Zeng, Recent progress in 2D group-VA semiconductors: from theory to experiment, Chem. Soc. Rev. 47, 982 (2018).

[19] R. Gui, H. Jin, Y. Sun, X. Jiang, and Z. Sun, Two-dimensional group-VA nanomaterials beyond black phosphorus: synthetic methods, properties, functional nanostructures and applications, J. Mater. Chem. A **7**, 25712 (2019).

[20] P. Schüelgen, D. Rosenbach, C. Li, T. W. Schmitt, M. Schleenvoigt, A. R. Jalil, S. Schmitt, J. Kölzer, M. Wang, B. Bennemann, U. Parlak, L. Kibkalo, S. Trellenkamp, T. Grap, D. Meertens, M. Luysberg, G. Mussler, E. Berenschot, N. Tas, A. A. Golubov, A. Brinkman, T. Schäpers, and D. Grützmacher, Selective area growth and stencil lithography for in situ fabricated quantum devices, Nat. Nanotechnol. **14**, 825 (2019).

[21] E. S. Walker, S. Muschinske, C. J. Brennan, S. R. Na, T. Trivedi, S. D. March, Y. Sun, T. Yang, A. Yau, D. Jung, A. F. Briggs, E. M. Krivoy, M. L. Lee, K. M. Liechti, E. T. Yu, D. Akinwande, and S. R. Bank, Composition-dependent structural transition in epitaxial $Bi_{1-x}Sb_x$ thin films on Si(111), Phys. Rev. Mater. **3**, 064201 (2019).